

## Variability and the size-luminosity relation of the intermediate mass AGN in NGC 4395

HOJIN CHO,<sup>1</sup> JONG-HAK WOO,<sup>1</sup> EDMUND HODGES-KLUCK,<sup>2,3,4</sup> DONGHOON SON,<sup>1</sup> JAEJIN SHIN,<sup>1,5</sup> ELENA GALLO,<sup>2</sup>  
HYUN-JIN BAE,<sup>1,6</sup> THOMAS G. BRINK,<sup>7</sup> WANJIN CHO,<sup>1</sup> ALEXEI V. FILIPPENKO,<sup>7</sup> JOHN C. HORST,<sup>8</sup> DRAGANA ILIĆ,<sup>9</sup>  
MICHAEL. D. JONER,<sup>10</sup> DAEUN KANG,<sup>1</sup> WONSEOK KANG,<sup>11</sup> SHAI KASPI,<sup>12</sup> TAEWOO KIM,<sup>11,13</sup> ANDJELKA B. KOVAČEVIĆ,<sup>9</sup>  
SAHANA KUMAR,<sup>7</sup> HUYNH ANH N. LE,<sup>1,14</sup> A. E. NADZHIP,<sup>15</sup> FRANCISCO POZO NUÑEZ,<sup>16</sup> V.G. METLOV,<sup>15</sup>  
V. L. OKNYANSKY,<sup>15</sup> SONGYOUN PARK,<sup>1</sup> LUKA Č. POPOVIĆ,<sup>17</sup> SUVENDU RAKSHIT,<sup>18,1,19</sup> MALTE SCHRAMM,<sup>20</sup>  
N. I. SHATSKY,<sup>15</sup> MICHELLE SPENCER,<sup>10</sup> EON-CHANG SUNG,<sup>21</sup> HYUN-IL SUNG,<sup>21</sup> A. M. TATARNIKOV,<sup>15</sup> AND OLIVER VINCE<sup>17</sup>

<sup>1</sup>*Department of Physics & Astronomy, Seoul National University, Seoul 08826, Republic of Korea*

<sup>2</sup>*Department of Astronomy, University of Michigan, Ann Arbor, MI 48109, USA*

<sup>3</sup>*Department of Astronomy, University of Maryland, College Park, MD 20742, USA*

<sup>4</sup>*NASA/GSFC, Code 662, Greenbelt, MD 20771, USA*

<sup>5</sup>*Major in Astronomy and Atmospheric Sciences, Kyungpook National University, Daegu 41566, Korea*

<sup>6</sup>*Department of Astronomy, Yonsei University, Seoul 03722, Republic of Korea*

<sup>7</sup>*Department of Astronomy, University of California, Berkeley, CA 94720-3411, USA*

<sup>8</sup>*San Diego State University, San Diego, CA 92182, USA*

<sup>9</sup>*Department of Astronomy, Faculty of Mathematics, University of Belgrade Studentski trg 16, Belgrade, 11000, Serbia*

<sup>10</sup>*Department of Physics and Astronomy, N283 ESC, Brigham Young University, Provo, UT 84602, USA*

<sup>11</sup>*National Youth Space Center, Goheung 59567, Republic of Korea*

<sup>12</sup>*School of Physics and Astronomy and Wise Observatory, Tel-Aviv University, Tel-Aviv 6997801, Israel*

<sup>13</sup>*Department of Astronomy and Space Science, Chungbuk National University, Cheongju 28644, Korea*

<sup>14</sup>*Department of Astronomy, University of Science and Technology, Hefei 230026, China*

<sup>15</sup>*Sternberg Astronomical Institute, M.V. Lomonosov Moscow State University, Universitetski pr. 13, 119234 Moscow, Russia*

<sup>16</sup>*Haifa Research Center for Theoretical Physics and Astrophysics, University of Haifa, Haifa, Israel*

<sup>17</sup>*Astronomical Observatory Belgrade; Volgina 7; 11000 Belgrade, Serbia*

<sup>18</sup>*Indian Institute of Astrophysics, Block II, Koramangala, Bangalore-560034, India*

<sup>19</sup>*Finnish Centre for Astronomy with ESO (FINCA), University of Turku, Quantum, Vesilinnantie 5, FI-20014 University of Turku, Finland*

<sup>20</sup>*National Astronomical Observatory of Japan, Mitaka, Tokyo 181-8588, Japan*

<sup>21</sup>*Korea Astronomy and Space Science Institute, Daejeon 34055, Republic of Korea*

## ABSTRACT

We present the variability study of the lowest-luminosity Seyfert 1 galaxy NGC 4395 based on the photometric monitoring campaigns in 2017 and 2018. Using 22 ground-based and space telescopes, we monitored NGC 4395 with a  $\sim 5$  minute cadence during a period of 10 days and obtained light curves in the UV, V, J, H, and K/Ks bands as well as the H $\alpha$  narrow-band. The RMS variability is  $\sim 0.13$  mag on *Swift*-UVM2 and V filter light curves, decreasing down to  $\sim 0.01$  mag on K filter. After correcting for continuum contribution to the H $\alpha$  narrow-band, we measured the time lag of the H $\alpha$  emission line with respect to the V-band continuum as  $55^{+27}_{-31}$  to  $122^{+33}_{-67}$  min. in 2017 and  $49^{+15}_{-14}$  to  $83^{+13}_{-14}$  min. in 2018, depending on the assumption on the continuum variability amplitude in the H $\alpha$  narrow-band. We obtained no reliable measurements for the continuum-to-continuum lag between UV and V bands and among near-IR bands, due to the large flux uncertainty of UV observations and the limited time baseline. We determined the AGN monochromatic luminosity at  $5100\text{\AA}$   $\lambda L_{\lambda} = (5.75 \pm 0.40) \times 10^{39} \text{ erg s}^{-1}$ , after subtracting the contribution of the nuclear star cluster. While the optical luminosity of NGC 4395 is two orders of magnitude lower than that of other reverberation-mapped AGNs, NGC 4395 follows the size-luminosity relation, albeit with an offset of 0.48 dex ( $\geq 2.5\sigma$ ) from the previous best-fit relation of Bentz et al. (2013).

## 1. INTRODUCTION

The origin of supermassive black holes is a subject of intensive research, including theoretical investigations on the black hole seeds in various mass scales (e.g., Volonteri et al. 2003, 2008; Barai & de Gouveia Dal Pino 2019). Direct observational evidence of the fossil record of either light or heavy seeds at high- $z$  is currently unavailable. The grown stage of supermassive black holes and their occupation fraction have been investigated to unveil the growth history of supermassive black holes (e.g., Miller et al. 2015; Gallo & Sesana 2019; Reines et al. 2013).

While the mass of the dynamically confirmed supermassive black holes is typically larger than a million solar mass in the present-day universe, it is unclear whether a population of intermediate mass black holes exist at the center of less massive galaxies (e.g., Greene 2012). It is observationally challenging to reveal the presence of intermediate mass black holes, as the dynamical measurements suffer from a limited spatial resolution even with the best available observational facilities. To probe the sphere of influence of an intermediate mass black hole, i.e.,  $M_{\bullet} \ll 10^6 M_{\odot}$  (i.e.,  $R_{\text{inf}} = GM_{\bullet}/\sigma_*^2$ , where  $\sigma_*$  is stellar velocity dispersion), typically a resolution better than 1 pc scale is required. For example, Nguyen et al. (2017) reported an upper limit of  $1.5 \times 10^5 M_{\odot}$  of the central black hole in NGC 404 based on the dynamical measurements with  $\sim 1$  pc scale resolution, demonstrating the challenge of finding dynamical evidence of intermediate mass black holes. There have been dynamical mass measurements or upper limits of intermediate mass black holes for only a small number of local galaxies (den Brok et al. 2015; Nguyen et al. 2018, 2019; Greene et al. 2019). While there are also various reports on intermediate mass black holes, for example, in ultraluminous X-ray sources (e.g., Mezcua et al. 2018), the origin of supermassive black holes is more closely related to the black holes at the galaxy centers, which are believed to be connected with their host galaxies in the growth history over the Hubble time (Kormendy & Ho 2013).

The nearby galaxy NGC 4395 at a distance of 4.6 Mpc (Karachentsev et al. 2003) is a unique test-bed for studying intermediate mass black holes. As a Seyfert 1 galaxy, NGC 4395 hosts an active galactic nucleus (AGN) with extremely low luminosity, as the bolometric luminosity is typically reported as below  $10^{41} \text{ erg s}^{-1}$  (e.g., Filippenko & Sargent 1989; Filippenko et al. 1993; Filippenko & Ho 2003; Lira et al. 1999; Moran et al. 1999). The host galaxy is classified as a dwarf galaxy with a stellar mass  $10^9 M_{\odot}$  (Filippenko & Sargent 1989; Reines et al. 2013) and there is no clear sign of a bulge while

a bar-like central structure is identified (den Brok et al. 2015). Various studies determined the mass of the central black hole in NGC 4395. For example, Filippenko & Ho (2003) estimated  $M_{\bullet} = 1.3 \times 10^4 M_{\odot}$  using the broad line region (BLR) size-luminosity relation from Kaspi et al. (2000). Edri et al. (2012) also reported  $M_{\bullet} = (4.9 \pm 2.6) \times 10^4 M_{\odot}$  based on the reverberation mapping analysis of Balmer broad emission lines using broad-band photometry (see also Desroches et al. 2006). On the other hand, Peterson et al. (2005) reported a higher mass  $M_{\bullet} = (3.6 \pm 1.1) \times 10^5 M_{\odot}$  using  $C_{\text{IV}}$  line reverberation mapping.

Recently, Woo et al. (2019) reported the mass of the central black hole in NGC 4395 as  $M_{\bullet} = 9100^{+1500}_{-1600} M_{\odot}$  based on reverberation mapping analysis, using narrow-band photometry. The reported time lag of the  $H\alpha$  emission, 83 min., is longer than that of the  $C_{\text{IV}}$  emission line, 48-66 min., (Peterson et al. 2005), suggesting consistency with the stratification of the BLR, which leads to a factor of  $\sim 2$  longer lag for  $H\alpha$  than  $C_{\text{IV}}$ . In contrast, Woo et al. (2019) measured the line dispersion velocity of  $H\alpha$  to be  $\sigma = 426 \pm 1 \text{ km s}^{-1}$ , while the line dispersion velocity of  $C_{\text{IV}}$  was reported as  $\sigma \sim 2900 \text{ km s}^{-1}$  by Peterson et al. (2005). Therefore, the main discrepancy of the black hole mass between  $H\alpha$ -based and  $C_{\text{IV}}$ -based reverberation mapping results is from the line width measurements. There have been various studies investigating the systematic difference between  $H\beta$ - and  $C_{\text{IV}}$ -based black hole masses, and in general  $C_{\text{IV}}$ -based mass suffers more uncertainties (e.g., Park et al. 2013; Denney et al. 2013).

While NGC 4395 presents an intermediate-mass black hole and low luminosity, the Eddington ratio of NGC 4395 is  $\sim 5\%$  (Woo et al. 2019), which is comparable to that of other reverberation-mapped AGNs. Therefore, it provides a useful test-bed for investigating the effect of luminosity vs. accretion rate on AGN properties, i.e., BLR stratification, non-virial motion, X-ray spectral energy distribution, etc.

As the lowest-luminosity Seyfert 1 galaxy known today, NGC 4395 also provides an interesting opportunity to investigate the photoionization and the size-luminosity relation at the low-luminosity regime. The size-luminosity relation has been studied with AGNs with optical luminosity at  $5100\text{\AA}$  larger than  $10^{42} \text{ erg s}^{-1}$  (Bentz et al. 2013), while it is yet to be probed whether the photoionization assumption is valid at extremely low luminosity.

In this study, we present variability analysis using data from our NGC 4395 monitoring campaign in 2017 and 2018, which include the UV, optical, and near IR photometry. We investigate the effect of the continuum on

the narrow-band light curves for constraining the validity of the lag measurements. Also, we investigate the BLR size-luminosity relation (Bentz et al. 2013) at the extreme low-luminosity end by combining NGC 4395 with previous reverberation results of AGNs with measured supermassive black holes. In section 2, we describe the observations and data reduction processes, and we present the data analysis in section 3. We compare our results with previously published results and discuss the BLR radius-luminosity relation in section 4. Our results are summarized in section 5. We assume the distance to NGC 4395 to be 4.4 Mpc throughout this paper, as adopted by den Brok et al. (2015).

## 2. OBSERVATION AND DATA REDUCTION

In 2017 and 2018 we performed intensive monitoring campaigns using 22 ground-based and one space telescope in order to obtain consecutive light curves of the AGN continuum flux and H $\alpha$  emission line flux over a couple of days time scale. The time lag of the H $\alpha$  emission line with respect to the V-band continuum is roughly estimated to be 1-4 hours based on the monochromatic luminosity at 5100Å, and the H $\beta$  size-luminosity relation (Bentz et al. 2013). Thus, a period of approximately one day (i.e., 24 hours) of observations is required to obtain a long enough time baseline to track the time lag between the V-band and H $\alpha$  light curves properly. Therefore, we combined multiple telescopes in various longitudes to fill in the day time gap in each telescope. The details of the participating observatories along with their telescopes and instruments are summarized in Table 1.

The campaign was carried out from 28th April to 5th May in 2017 (all dates are presented in UT), and from 6th to 9th April in 2018, during which we used various filters which cover UV to near IR continuum.

### 2.1. Optical observations

In the optical range, we mainly used the V-band and narrow H $\alpha$ -band filters, while the B and R band filters were occasionally used for flux-calibration. As the time lag of the H $\alpha$  emission line with respect to the optical continuum is expected to be as short as less than one hour, a relatively short time cadence was required. For the continuum monitoring with the V-band filter, we mainly used 1-m class telescopes, while for the narrow H $\alpha$ -band monitoring we used  $\sim$ 2-m class telescopes to increase the S/N per exposure. Examples of the images of NGC 4395 taken from different telescopes and bands are shown in Figure 1. To ensure better than 1-2% flux measurement errors, we determined the optimal exposure time for each telescope based on the imaging data,

which were obtained before the start of the monitoring campaign. For example, we used 180 sec. exposure time for the V-band imaging with the MDM 2.4m telescope, while in general we used 300 sec. exposure time for both the V-band and the H $\alpha$ . Thus, we maintained  $\sim$ 5 min. time resolution at each telescope.

For the narrow H $\alpha$ -band observations, we used the MDM 1.3m, BOAO 1.8m, and MDM 2.4m telescopes in 2017. The weather at the MDM observatory was relatively good, while the data from BOAO suffered large uncertainties due to bad weather and low sensitivity, hence, these data were not used in the cross-correlation analysis. In 2018, we used the MDM 2.4m telescope for the narrow H $\alpha$ -band observations. Since we only used the H $\alpha$ -band data from the MDM 2.4m telescope for the time lag analysis, we present the response function of the narrow H $\alpha$ -filter in Figure 2, which covers a spectral range between 6470-6560Å, including the broad H $\alpha$  emission line along with the narrow [N II] and H $\alpha$  lines. Note that while the flux from emission lines is dominant in the narrow H $\alpha$ -band, there is a significant contribution from the continuum, which has to be corrected for in order to obtain the reliable lag of the H $\alpha$  emission line (see 3.3).

The standard data reduction was performed including bias subtraction and flat-fielding using IRAF procedures, and cosmic ray rejection using the L.A.Cosmic algorithm (van Dokkum 2001). If necessary, approximately 2-4 consecutive exposures were combined to construct a one-epoch image to decrease the photometric error to less than 5%, while the time resolution between epochs was kept at a maximum of 10 min. After that, data quality was assessed based on visual inspection, and any epoch with quality issues, i.e., failed tracking or trouble in the performance reported in the observing log was rejected from further photometry analysis.

### 2.2. UV Observations

We observed NGC 4395 using *Swift* UVOT to monitor the variability of the UV continuum and to investigate the time lag between continuum bands. The UVOT data were taken from 2017-04-28 to 2017-05-02 using the UVM2 filter, which is centered at 2231Å. Note that one orbital period of *Swift* is 96 minutes, of which NGC 4395 was visible for  $\sim$ 2000 sec. We performed the data reduction with HEASoft (Blackburn et al. 1999), including background subtraction, correction for anomalous zero exposures, and correction for the degradation of the UVOT sensitivity.

### 2.3. Near-Infrared Observations

We monitored NGC 4395 using J, H, and K/Ks filters at the Caucasus Mountain Observatory (CMO)

**Table 1.** Observing Facilities Participating in the Campaign

Observatory Name	Longitude	Aperture	Detector	Filters
Bohyunsan Optical Astronomy Observatory (BOAO)	128°58'E	1.8m	e2v CCD231-84	V, H $\alpha$
Mt. Laguna Observatory (MLO)	116°25'W	1m	e2V 42-40 2k	B, V
MDM Observatory (MDM)	111°37'W	1.3m	Templeton	B, V, H $\alpha$
		2.4m	MDM4K	V, H $\alpha$
Mt. Lemmon Optical Astronomy Observatory (LOAO)	110°47'W	1.0m	e2v CCD 231-84	B, V
West Mountain Observatory (WMO)	111°50'W	0.9m	FLI-PL3041-UV	B, V
Caucasus Mountain Observatory (CMO)	42°40'E	0.6m	Aspen CG42	B, V
		2.5m	HAWAII 2-RG	J,H,K
Astronomical Station Vidojevica (ASV)	21°33'E	1.4m	Apogee U42	B, V
Sobaeksan Optical Astronomy Observatory (SOAO)	128°27'E	0.61m	e2v CCD42-40	B, V
Vainu Bappu Observatory (VBO)	78°49'E	1.3m	Apogee Aspen CG42	B, V
Higashihiroshima Astronomical Observatry (Hiroshima)	132°47'E	1.5m	HOWPol	B, V, R
LCOGT - McDonald (McDonald)	104°01'W	1m	Sinistro	V
LCOGT - Haleakala (Haleakala)	156°15'W	0.4m	SBIG 6303	V
Lick Observatory (Nickel)	121°39'W	1m	Direct Imaging Camera CCD-2	B, V
Wise Observatory (Wise)	34°46'E	1m	STX-16803	B, V, H $\alpha$
		0.7m	FLI-PL16801	B, V
Cerro Tololo Inter-American Observatory (CTIO)	70°48'W	0.6m	SBIG STL-11000M	V, H $\alpha$
Okayama Astrophysical Observatory (OAO)	133°36'E	0.91m	OAO/WFC	K <sub>s</sub>
Deokheung Optical Astronomy Observatory (DOAO)	127°27'E	1m	PL-16803 <sup>a</sup>	B, V
			SOPHIA-2048B <sup>b</sup>	B, V
Dark Sky Observatory (DSO)	81°25'W	0.36m	Apogee Alta U47	V
<i>Swift</i> Ultraviolet/Optical Telescope (UVOT)	<i>satellite</i>	0.3m	Intensified CCD	UVM2
Gemini Observatory - North	155°28'W	8.1m	GMOS-N	g, Spectroscopy

<sup>a</sup>Used in 2017<sup>b</sup>Used in 2018

2.5m telescope (the ASTRONIRCAM instrument, [Nadjić et al. 2017](#)) and Okayama Astrophysical Observatory (OAO) 0.91m telescope (OAO/WFC, [Yanagisawa et al. 2019](#)). At the CMO 2.5m, we used the K band filter of the Mauna Kea Observatory (MKO) system for 3 nights in 2017. In addition, J and H band filters were occasionally used during the monitoring. In the case of OAO observations, we used the K<sub>s</sub> filter, but the image quality was too poor to perform further analysis.

#### 2.4. Optical spectroscopic Observations

In addition to the photometric observations, we also performed spectroscopic observations for  $\sim 3.5$  hours, using the Gemini Multi-Object Spectrograph (GMOS) on Gemini North telescope on 29th April 2017. Initially, we planned to observe NGC 4395 for two consecutive nights in 2017 (GN-2017A-Q2, PI: Woo), and 3 nights in 2018 (GN-2018-Q102, PI: Woo), but all scheduled nights were lost due to snowstorms. Nevertheless, we were able to monitored the target for  $\sim 3.5$  hours under varying cloudy conditions on 29th April 2017.

We used a long-slit with a 0.75" slit-width and the R831 grating, obtaining spectral resolution of  $R = 2931$ ,



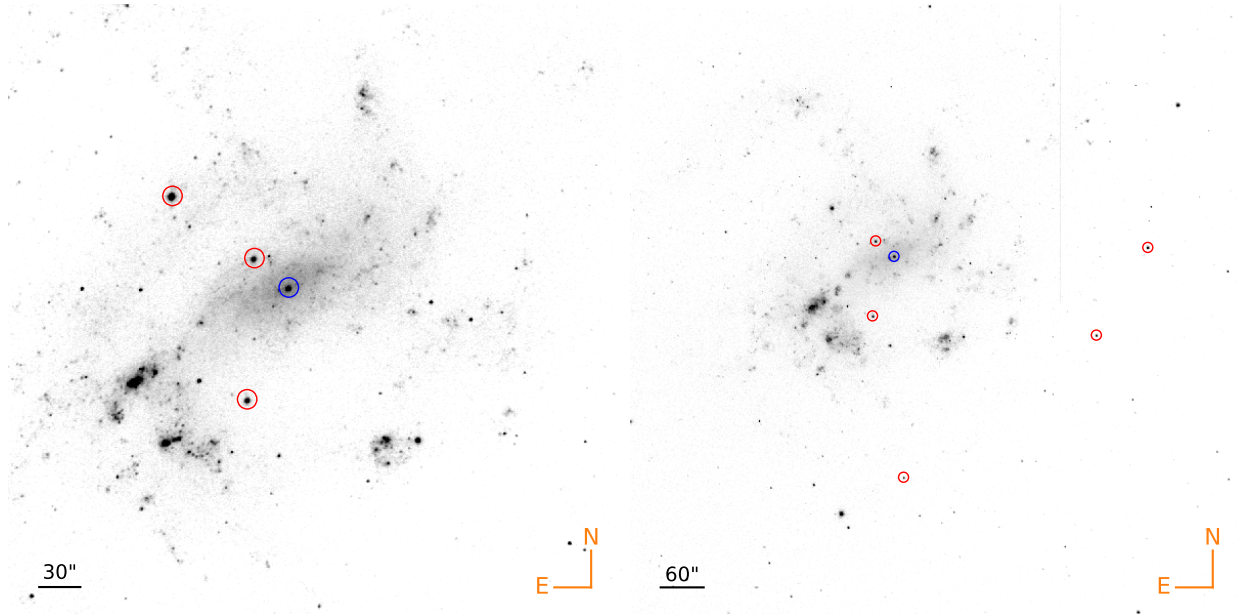


**Figure 1.** *Left:* An example of V-band images of NGC 4395 with 300 sec. exposure, obtained at the MDM 1.3 m telescope. Three comparison stars are marked with red circles, while the target AGN is denoted with a blue circle. The field of view is  $7.6' \times 7.6'$  after cropped, and the radius of the circle corresponds to the aperture size of  $4''$  for differential photometry. *Right:* An example of the  $H\alpha$  narrow-band images of NGC 4395 with field of view  $14.3' \times 14.3'$  after cropped, obtained at the MDM 2.4m telescope. The blue circle denotes the AGN, whereas red circles mark 5 comparison stars. The field of view is shown after trimming the shadow of the guide probe and the vignetted region. The radius of the circle corresponds to the aperture size of  $7''$  for differential photometry.

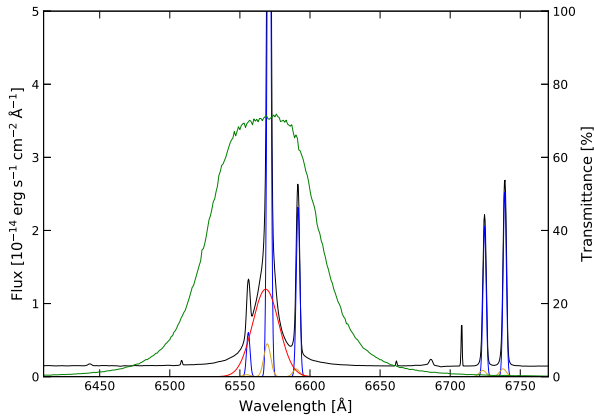


**Figure 2.** The response function of the KP1468 filter available at the MDM 1.3m telescope (green line). The spectrum of NGC 4395 obtained with the Gemini GMOS is compared with the response function. Note that the emission lines were decomposed into broad  $H\alpha$  (red) and wing (yellow) and core (blue) of the narrow lines (i.e.,  $H\alpha$ ,  $[N II]$ ,  $[S II]$ ).

which was good enough to resolve the broad and narrow components of  $H\alpha$ , and the wing and core components of the narrow lines, i.e.,  $[N II]$  and  $[S II]$  as presented by Woo et al. (2019). The instrument set-up covered the spectral range  $4606\text{\AA}$  to  $6954\text{\AA}$ , with a  $0.374\text{ \AA pix}^{-1}$  scale. We set the position angle to be  $50.2$  degrees East

from North. We used 2-pixel binning along the spatial direction, resulting in  $0.16''\text{ pix}^{-1}$  scale. Each exposure was 300 sec. long and we obtained a high-quality spectrum every 6 min., including 1 min. overhead per exposure. A total of 36 epochs was obtained during the 3.5-hour run, while three epochs were discarded due to strong cosmic rays on top of the  $H\alpha$  line. Additionally we observed G191-B2B for flux calibration purpose (Massey et al. 1988; Massey & Gronwall 1990; Bohlin et al. 1995).

We performed standard data reduction with the Gemini IRAF package, including bias subtraction, flat field, wavelength calibration, and flux calibration. Cosmic rays were rejected using L.A.Cosmic routine (van Dokkum 2001). From each exposure, we extracted a one-dimensional spectrum using an aperture size, which was three times the seeing FWHM, in order to compensate for varying seeing during the observing run. Out of the 33 epochs, two consecutive spectra showed relatively low S/N and we averaged these two epochs. Thus, we finalized a total of 32 spectra.

To obtain the flux of the broad  $H\alpha$  emission line, we performed decomposition analysis as outlined by Woo et al. (2019). In brief, we modeled the  $[SII]\lambda 6717, 6731$  doublet using two Gaussian components for each line since both  $[SII]$  lines show a broad wing component and a narrow core component. For the continuum subtrac-

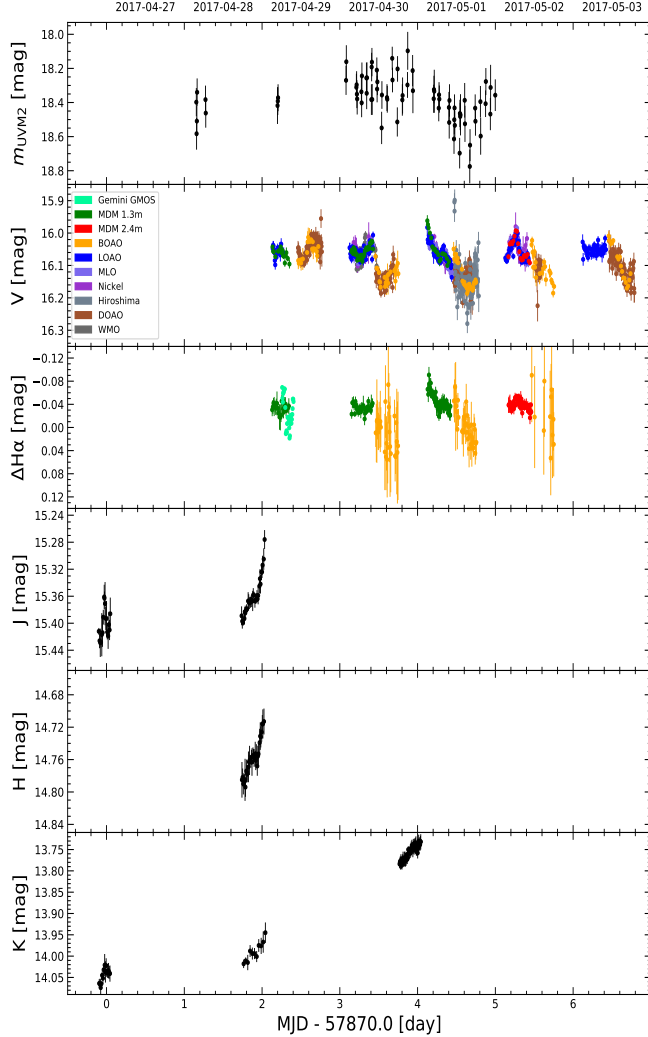


**Figure 3.** Light curves in UV, optical (V and  $H\alpha$ ), and near-IR bands (J, H, and K) obtained in 2017. For the optical data, we only present the light curves from 10 telescopes with good weather condition during the observations and the mean error in V band photometry less than 0.03 magnitude.  $H\alpha$  panel shows light curves obtained from  $H\alpha$  narrow-band filter, as well as a light curve obtained from GMOS spectral modeling. All errors shown here are  $1-\sigma$  errors.

tion, we used a straight line using the continuum flux around  $6660\text{\AA}$ - $6700$  and  $6760\text{\AA}$ - $6800\text{\AA}$  ranges. By assuming that line profile and flux of [SII] was constant during the night, we performed calibration for flux, spectroscopic resolution, and wavelength shift, so that the [SII] $\lambda 6717, 6731$  model profile of each epoch remains constant. Also, we constructed mean and RMS spectra using the calibrated spectra. Then, we modeled the  $H\alpha$  and [NII] region by assuming that the narrow  $H\alpha$  line and [NII] $\lambda 6548, 6583$  doublet have the same profile as that of [SII] $\lambda 6717, 6731$ . For each epoch, we modeled the broad  $H\alpha$  line with a single Gaussian profile, and

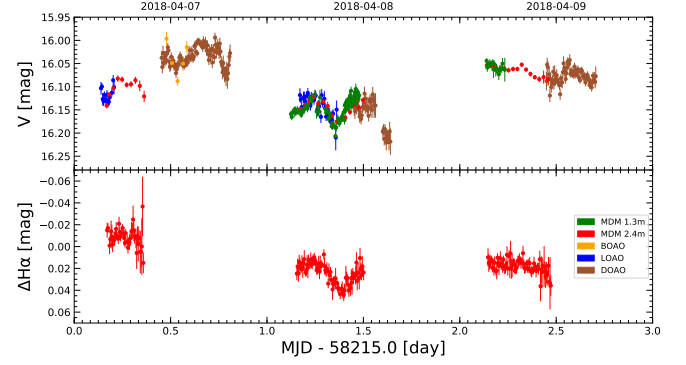


**Figure 4.** V (*top*) and  $H\alpha$  (*bottom*) light curves obtained in 2018. We only show the light curves from 5 telescopes with good weather condition during the observations and average error in V band light curve less than 0.03 magnitude. All errors shown here are  $1-\sigma$  errors.

the narrow lines, i.e.,  $H\alpha$  and [NII] with the same profile obtained for [SII]. In addition, we used a linear line for the continuum. We simultaneously fitted emission lines and continuum in the spectral range of  $6450\text{\AA}$ - $6670\text{\AA}$ . We obtained the light curve of the broad  $H\alpha$  line flux as shown in the 2nd panel in Figure 3. Note that the  $\sim 3.5$ -hour baseline is too short to reliably measure the time lag between the continuum and the broad emission line (see 3.4).

### 3. ANALYSIS

#### 3.1. Differential Photometry

To measure the flux variability of the AGN continuum and  $H\alpha$  emission line, we first performed aperture photometry, using the `photutils` package (Bradley et al. 2017). Since the majority of images showed seeing variation during the night, we matched the point-spread function (PSF) before performing aperture photometry. The PSF was constructed based on isolated, bright, and unsaturated stars in each image, which were subsequently convolved so that all images have the same matched PSF, which was obtained from the worst seeing image of the night, typically  $1.5\text{--}4''$ . Using the PSF-matched images, we then performed aperture photometry for the target AGN and comparison stars in the FoV. A global background image was constructed using the `SExtractorBackground` estimator of the `photutils` package, which was subtracted from each image. In addition, we determined the residual background for individual sources using annuli with an outer radius, which was determined between 3 and 5 times of the seeing FWHM, and an inner radius, which was between 2 and 3 times of the seeing FWHM. Then, the calculated residual background value was taken from the median value measured within the aperture. We note that the resid-

ual background flux is insignificant and the additional background subtraction did not change the flux of most of the comparison stars. In contrast, this process was required for NGC 4395, since the host galaxy contribution at the galactic center was significant. Consequently, the additional subtraction lowered the AGN flux.

We determined the aperture size to include more than 99% of the point source flux. Then, we performed differential photometry for a number of nearby comparison stars. Depending on the FoV of each camera at each telescope, we selected various number of stars (i.e., 3 to 8 stars for each set of observations), which were non-varying and unsaturated bright stars with photometry error less than 2%. To identify variable stars, we used the table from [Thim et al. \(2004\)](#). In Figure 1, we present an example of the V-band and H $\alpha$ -band images along with the selected comparison stars. We calculated the difference between the instrumental magnitude and the known magnitude of each comparison star, and adopt the mean difference as the relative normalization value ( $\delta V$ ) for each epoch. We assumed the standard deviation of the  $\delta V$  from individual comparison stars as a systematic error of the normalization, which was added to the error of the instrumental magnitude and error from the background flux for calculating a total error.

Based on the aperture photometry and calibration, we constructed light curves by combining measurements from different telescopes. In this process, we inter-calibrated the light curves in order to avoid a systematic offset between light curves obtained from different telescopes due to the difference in the response function of the filters, detector efficiency, etc. We matched each light curve with a reference light curve by adding a linear shift in magnitude. In other words, the mean magnitude within the overlapped time interval in a light curve was forced to be the same as that of the reference light curve.

### 3.1.1. Detailed Inter-calibration Information

For the light curve of 2017-04-30, WMO, MLO, and BOAO data were inter-calibrated with each other as the light curve of WMO overlaps with the light curve from the other two telescopes. We applied the same correction to those of the MLO and BOAO on other nights. The light curves of MDM 1.3m on 2017-04-30 and 2017-05-01 were calibrated with respect to those of MLO on respective nights, and the average correction shift for MDM 1.3m was applied to its light curve of 2017-04-28 UT. Finally, any light curve that overlapped with BOAO were calibrated with respect to BOAO, while any light curve that overlapped with MLO or MDM 1.3m were calibrated to them, respectively.

For the 2018 data, we calibrated light curves of DOAO with respect to those of MDM 2.4m on 2018-04-08 UT and 2018-04-09 UT, and the average correction factor shift was applied to the light curve of DOAO 2018-04-07. Other light curves were calibrated with respect to either MDM 2.4m or DOAO depending on which light curve they overlap the most. Finally, we calculated V-band zero points using the bright nearby star 2MASS J12255090+3333100, whose V-band magnitude was determined as  $V_* = 16.9$  by converting the  $u'g'r'i'z'$  magnitudes from Sloan Digital Sky Survey Data Release 12 (SDSS DR12) based on the equations of [Jester et al. \(2005\)](#). Comparing with the instrumental magnitude of the comparison star, we obtained the normalization and applied it to the V-band light curve obtained with the MDM 2.4m telescope on 2017-05-02 and 2018-04-08, and all other inter-calibrated light curves were adjusted accordingly.

Photometric H $\alpha$  light curves were not inter-calibrated in the same manner as the V-band was calibrated since their light curves did not overlap with each other, and for the same reason, inter-calibration did not affect the relative photometry of H $\alpha$ . We only shifted the light curve of the H $\alpha$  broad component from Gemini GMOS spectroscopic observation to match that of the MDM 1.3m.

### 3.1.2. Light Curves

In Table 2, Figure 3, and Figure 4, we present the calibrated light curves of the V-band and H $\alpha$ -band, after excluding the data obtained with bad weather since the error bars are too large to provide any meaningful measurements. Overall, the two curves show similar trends, which demonstrate correlated variability. However, most segments of the V-band light curve are not suitable for reverberation-mapping analysis due to 1) the lack of corresponding H $\alpha$  observations, 2) the weak variability in the H $\alpha$ -band light curve, and 3) large uncertainty of the H $\alpha$  photometry. Among the monitoring data obtained in 2017 and 2018, we identified only two nights, 2017-05-02 and 2018-04-08, from which we were able to achieve reliable time lag measurements. We will focus on these two nights for further reverberation-mapping analysis in Section 3.3.1.

For the data obtained with the *Swift* UVM2 filter, we binned event files into 300 sec. exposures and measured the count rate from the circular apertures of 3" radii in order to maximize the S/N. Then, photon count rates,  $\dot{\gamma}$ , were corrected for the large-scale sensitivity gradient and converted into AB magnitudes as  $m_{\text{UVM2}} = -2.5 \log_{10} \dot{\gamma} + 18.54$  ([Breeveld et al. 2011](#)). Finally, aperture correction to the standard UVOT aper-

**Table 2.** Photometry Data

MJD-50000.0	Band	Magnitude	Uncertainty	Notes
(1)	(2)	(3)	(4)	(5)
7869.90099	J	15.412	0.005	
7869.90569	K	14.064	0.010	
7869.91038	J	15.426	0.011	
7869.91508	K	14.065	0.012	
7869.91931	J	15.429	0.021	

NOTE—Columns are (1) Modified Julian date, (2) band, (3) magnitude, (4)  $1\text{-}\sigma$  uncertainty in magnitude (5) note. (This table is available in its entirety in machine-readable form.)

ture of  $5''$  was applied using on-field stars in each temporal bin in order to convert aperture magnitude into PSF magnitude.

For J, H, and K band images, AGN magnitudes were obtained for each exposure by performing photometry with circular apertures of  $2.2''$  diameter, with respect to the comparison star 2MASS J12255090+3333100, whose magnitude in each band is  $J = 14.362$ ,  $H = 13.939$ , and  $K = 13.786$  when converted to MKO system.

### 3.2. Variability

We quantified the variability of NGC 4395 using the light curves presented in Figures 3 and 4. We calculated the RMS variability in magnitude ( $\sigma_m$ ), the ratio between the maximum flux and minimum flux ( $R_{\max}$ ), and the fractional variability ( $F_{\text{var}}$ ), using 2017 and 2018 light curves, respectively. The fractional variability  $F_{\text{var}}$  is defined as

$$F_{\text{var}} = \frac{1}{\langle f \rangle} \sqrt{\langle f^2 \rangle - \langle f \rangle^2 - \langle \epsilon_f^2 \rangle} \quad (1)$$

(Vaughan et al. 2003) where  $f$  is the flux at each epoch,  $\langle f \rangle$  is the mean flux, and  $\epsilon_f$  is the flux error. The error of the fractional variability is given by

$$\epsilon(F_{\text{var}}) = \sqrt{\left( \sqrt{\frac{1}{2N}} \frac{\langle \epsilon_f^2 \rangle}{\langle f \rangle^2 F_{\text{var}}} \right)^2 + \left( \sqrt{\frac{\langle \epsilon_f^2 \rangle}{N}} \frac{1}{\langle f \rangle} \right)^2} \quad (2)$$

where  $N$  is the number of epochs.

Table 3 summarizes the variability measurements. Using the light curves obtained in 2017, we find RMS variability from 0.02 to 0.13 mag. in the continuum, and

the 2018 data show a similar range.  $R_{\max}$  of the continuum band ranges from 1.08 to 1.87 in 2017 and similar values in 2018. Accounting for the measurement errors in the light curves from 2017, we find that the fractional RMS variability ranges from 1% to 8%, with a decreasing trend with an increasing wavelength of the continuum. The exception is the UVM2 band, which shows a similar fractional variability compared to V-band, due to the larger uncertainty of the UV photometry. In general, we find similar trends in the light curves obtained in 2018.

To compare the variability with the consistent length of the time baseline, we calculated the variability statistics of the near-IR bands using the light curves obtained on 2017-04-28. RMS deviation,  $R_{\max}$  variability, and fractional variability show a clear decreasing trend with the increasing wavelength.

We also used the data from 2017-05-02 and 2018-04-08 to measure the variability in the V-band and  $H\alpha$  narrow-band respectively for comparison. We obtained RMS variability of 0.01 mag.,  $R_{\max}$  of 1.1, and fractional RMS variability of 1-2%. Note that since the narrow-band contains non-variable narrow lines, i.e., [NII] and narrow  $H\alpha$  emission lines which account for 49% of the total flux observed in the  $H\alpha$  narrow-band (see 3.3), the actual variability amplitude is a factor of 3 higher than these measurements. We also measured the variability of the entire  $H\alpha$  light curves of 2017 and 2018, and obtained  $\sigma_{m, H\alpha} = 0.012$ ,  $R_{\max, H\alpha} = 1.07$ , and  $F_{\text{var}, H\alpha} = 0.006$  in 2017 and  $\sigma_{m, H\alpha} = 0.015$ ,  $R_{\max, H\alpha} = 1.08$ , and  $F_{\text{var}, H\alpha} = 0.012$  in 2018, which are broadly consistent with single-night values with continuum correction.

### 3.3. Continuum Correction for $H\alpha$ Photometry

Ideally, spectroscopic monitoring can provide better data to measure the  $H\alpha$  emission line flux by separating the emission line from the continuum based on the spectral decomposition, leading to less uncertainty of the cross-correlation analysis between AGN continuum and  $H\alpha$  emission line. The main uncertainty of photometric reverberation-mapping comes from the fact that the contribution from the AGN continuum to the total flux obtained with a broad filter has to be properly determined (Desroches et al. 2006). Compared to a broad-band filter, the narrow  $H\alpha$ -band filter contains less AGN continuum and can be effectively used for the  $H\alpha$  emission line flux monitoring. If the continuum contribution in the narrow-band  $H\alpha$  filter can be properly corrected for, narrow-band photometry can lead to successful measurements of the  $H\alpha$  emission line flux. In this section, we investigate the effect of the variability of the continuum in the  $H\alpha$  band.



**Table 3.** Variability Statistics

Band	Central Wavelength ( $\mu\text{m}$ )	$\sigma_m$ (mag)	$R_{\text{max}}$	$F_{\text{var}}$ (%)
2017				
UVM2	0.225	0.13	1.87	$8.1 \pm 1.2$
V	0.551	0.10	1.70	$8.2 \pm 0.1$
J	1.22	0.03	1.15	$2.7 \pm 0.2$
H	1.63	0.02	1.08	$1.6 \pm 0.3$
K	2.19	0.12	1.37	$1.1 \pm 0.1$
H $\alpha^a$	0.66	0.01	1.07	$0.6 \pm 0.1$
2018				
V	0.551	0.05	1.23	$4.7 \pm 0.1$
H $\alpha^b$	0.66	0.02	1.08	$1.2 \pm 0.1$
2017-04-28				
J	1.22	0.03	1.12	$2.4 \pm 0.2$
H	1.63	0.02	1.08	$1.6 \pm 0.3$
K	2.19	0.02	1.07	$1.2 \pm 0.6$
2017-05-02				
V	0.551	0.03	1.11	$2.5 \pm 0.1$
H $\alpha^b$	0.657	0.01	1.04	$0.1 \pm 0.4$
2018-04-08				
V	0.551	0.02	1.10	$1.7 \pm 0.1$
H $\alpha^b$	0.657	0.01	1.03	$0.6 \pm 0.1$

<sup>a</sup>Light curves from MDM 1.3m & MDM 2.4m

<sup>b</sup>Light curves from MDM 2.4m

### 3.3.1. Test of continuum variability for H $\alpha$ Photometry

The total flux measured with a narrow-band H $\alpha$  filter is composed of the flux from the broad H $\alpha$  line, narrow emission lines and the continuum emission from the AGN and its host galaxy. Thus, we model the narrow-band H $\alpha$  flux  $F_{\text{nH}\alpha}(t)$  as

$$F_{\text{nH}\alpha}(t) = f_{\text{BH}\alpha}(t) + f_{\text{cont}}(t) + f_{\text{NL}} \quad (3)$$

where  $f_{\text{BH}\alpha}(t)$  is the variable flux of the broad H $\alpha$  emission,  $f_{\text{cont}}(t)$  is the variable flux of the continuum from both AGN and non-varying stars, and  $f_{\text{NL}}$  is the non-varying flux from narrow emission lines. While the variability of  $f_{\text{BH}\alpha}(t)$  is delayed with respect to the V-band light continuum, the variability of  $f_{\text{cont}}(t)$  is similar to that of V-band. If we ignore the difference of the wave-

length between V-band and H $\alpha$ -band, the flux variability of  $f_{\text{cont}}(t)$  is to be coherent with that of V-band. This assumption is reasonable if there is no color variability in this relatively short wavelength range covered by V-band and H $\alpha$ -band. Furthermore, if there is no significant contribution from non-varying stars to the H $\alpha$  filter, then the variability amplitude of the continuum will be similar between V-band and H $\alpha$ -band spectral ranges.

A key for the proper continuum correction is to have a high-quality spectrum, with which the AGN continuum fraction can be reliably determined. We used the mean spectrum obtained with the Gemini GMOS during our 3.5-hour observing run, for measuring the flux contribution of each component based on the spectral decomposition. We modeled the GMOS spectrum with multiple components, the narrow H $\alpha$  emission line and [NII] $\lambda$ 6548, 6583 doublet, broad H $\alpha$  emission line, and the continuum. We used double Gaussian models for the narrow emission line to account for the core and wing components, a single Gaussian component for the broad H $\alpha$  emission line, and a first-order polynomial for the continuum (see Figure 2). After convolving each component with the response function of the KP1468 H $\alpha$  filter, we determined that the continuum is  $18.3 \pm 0.3\%$  of the total flux in the narrow-band H $\alpha$  filter, while the narrow line and broad line contribute 49% and 32% of the flux, respectively.

On the other hand, the variability amplitude of the continuum in the narrow-band H $\alpha$  filter can differ from that of the V band, if the variability amplitude depends on the continuum wavelength, while it is reasonable to assume the same amplitude, considering the small difference of the wavelengths between two filters. We model the continuum in the H $\alpha$  filter by quantifying the dimensionless variability amplitude  $K$  as

$$f_{\text{cont}}(t) = \left[ (1 - K) + K \frac{f_V(t)}{\langle f_V \rangle} \right] \langle f_{\text{cont}} \rangle \quad (4)$$

where  $\langle f_{\text{cont}} \rangle$  is the mean continuum flux in the H $\alpha$  filter,  $\langle f_V \rangle$  is the mean flux of the V-band filter, and  $f_V(t)$  is the V-band flux at each epoch. For example, if  $K = 1$ , then the variability amplitude of the continuum is the same between V-band and H $\alpha$ , while the continuum in the H $\alpha$  has no variability for  $K = 0$ . Thus, by parameterizing the variability amplitude by  $K$ , we can test the effect of the continuum contribution to the H $\alpha$  light curve. Different assumptions on variability amplitude would affect the recovered H $\alpha$  light curve as shown in Figure 5, where we present the change of the narrow-band H $\alpha$  filter light curve using  $K = 0, 0.5$ , and 1, respectively.

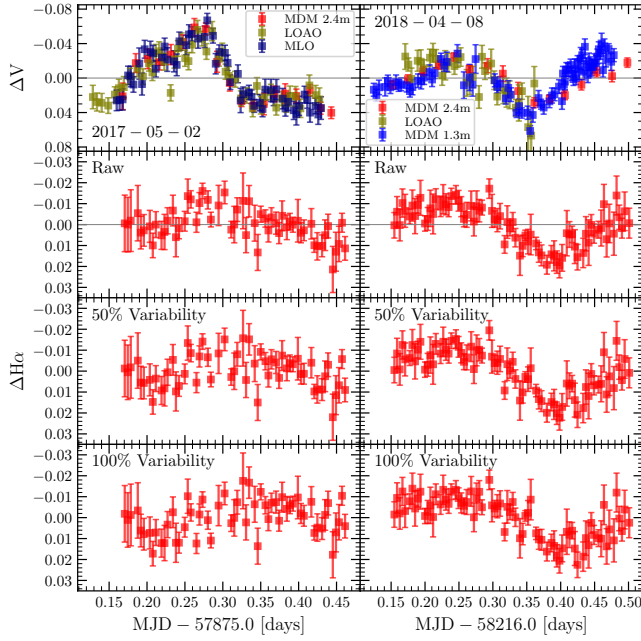


**Figure 5.** Light curves of V band (top) and narrow H $\alpha$  filter (bottom 3 panels) obtained on 2017-05-02 UT (left) and 2018-04-08 UT (right), using MDM telescopes, MLO, and LOAO. H $\alpha$  light curves with continuum subtracted are presented also, assuming continuum fraction of 18.3% of total H $\alpha$  flux on average and variability of 50% and 100% of that of V band light curves.

### 3.4. The Effect of Continuum Contribution on the Continuum-H $\alpha$ Time Lag

To quantify the effect of the continuum contribution in the H $\alpha$ -band on the time lag analysis, we used five H $\alpha$  light curves, which were corrected for the continuum contribution with an assumed variability amplitude (K in Eq. (4)).

For measuring a time lag from a pair of light curves (V-band and H $\alpha$ -band), we computed the interpolated cross-correlation function (ICCF; White & Peterson 1994) to measure the lag between the two light curves. We adopted the flux randomization/random subset selection method (FR/RSS; Peterson et al. 1998; see also Peterson et al. 2004) to estimate its uncertainty. The ICCF  $r(\tau)$  was computed over  $-4 \text{ hr} < \tau < 4 \text{ hr}$  with 0.01 hr interval. We obtained two ICCFs by interpolating either the V-band light curve or the H $\alpha$  light curve and then adopted the average of the two ICCFs. We simulated 2000 realizations with the FR/RSS. For each realization, we re-sampled each light curve by allowing any epoch to be drawn multiple times. Then the flux at each epoch was randomized with log-normal distribution corresponding to the measured flux, flux error, and the number of times that epoch was drawn in the

**Table 4.** Rest-frame Time Lags for Broad H $\alpha$  Line from Photometric Light Curves

Date (UT)	Continuum correction	$\tau_{ICCF}$ (min.)	$\tau_{zDCF}$ (min.)	$\tau_{JAV}$ (min.)
(1)	(2)	(3)	(4)	(5)
2017-05-02	no correction	$55^{+27}_{-31}$	$67^{+22}_{-32}$	$59^{+14}_{-14}$
	25% of V-band variability	$72^{+25}_{-33}$	$67^{+36}_{-21}$	$74^{+18}_{-14}$
	50% of V-band variability	$88^{+27}_{-44}$	$119^{+27}_{-37}$	$98^{+17}_{-22}$
	75% of V-band variability	$104^{+31}_{-55}$	$119^{+30}_{-20}$	$120^{+14}_{-22}$
	100% of V-band variability	$122^{+33}_{-67}$	$147^{+20}_{-32}$	$135^{+7}_{-52}$
2018-04-08	no correction	$49^{+15}_{-14}$	$33^{+24}_{-27}$	$68^{+11}_{-22}$
	25% of V-band variability	$56^{+13}_{-13}$	$67^{+4}_{-32}$	$76^{+36}_{-11}$
	50% of V-band variability	$64^{+14}_{-14}$	$67^{+23}_{-28}$	$84^{+28}_{-13}$
	75% of V-band variability	$73^{+14}_{-14}$	$67^{+30}_{-23}$	$94^{+29}_{-13}$
	100% of V-band variability	$83^{+13}_{-14}$	$99^{+9}_{-35}$	$100^{+18}_{-11}$
2017-04-29	no correction	$79^{+30}_{-25}$	$70^{+11}_{-16}$	-
2017-04-30	no correction	$84^{+86}_{-66}$	$131^{+29}_{-80}$	-
2017-05-01	no correction	$2^{+19}_{-14}$	$8^{+21}_{-16}$	-

NOTE—Time lag measurements after subtracting continuum contribution from the H $\alpha$  narrow-band flux. The continuum flux is on average 18.3 %, but varies as in the V-band variability. The time lag represents the median of the distribution for ICCF and JAVELIN, respectively, and the maximum likelihood lags for zDCF. Central 68% intervals are taken as their uncertainties.

re-sampling step. The centroid of ICCF, defined as the ICCF-weighted mean of  $\tau$  where  $r(\tau) > 0.8 r_{\text{max}}$ , was calculated for each realization. Finally, the median and the lower/upper bounds of the 68% central confidence interval of the centroid distribution were taken as the time lag and its lower/upper uncertainty. In addition, we used the  $z$ -transformed discrete correlate function (zDCF; Alexander 1997) and the JAVELIN method (Zu et al. 2011) to measure the time lag between V-band and H $\alpha$ -band light curves, in order to compare with the ICCF results. Our measurements on continuum-H $\alpha$  time lag are summarized on Table 4.

First, we present the ICCF, zDCF, and JAVELIN measurements using the best light curves from 2018-04-08 in Figure 6. We also used the light curves from 2017-05-02 for a consistency check. Without correcting for the continuum contribution to the H $\alpha$ -band, we obtained the ICCF time lag  $55^{+27}_{-31}$  min. from the 2017-05-02 data, and  $49^{+15}_{-14}$  min. for the 2018-04-08 data. These results are consistent with those of zDCF and JAVELIN measurements, where  $67^{+22}_{-32}$  min. (zDCF) and  $59^{+14}_{-14}$  min. (JAVELIN) were measured for the 2017-05-02 data and

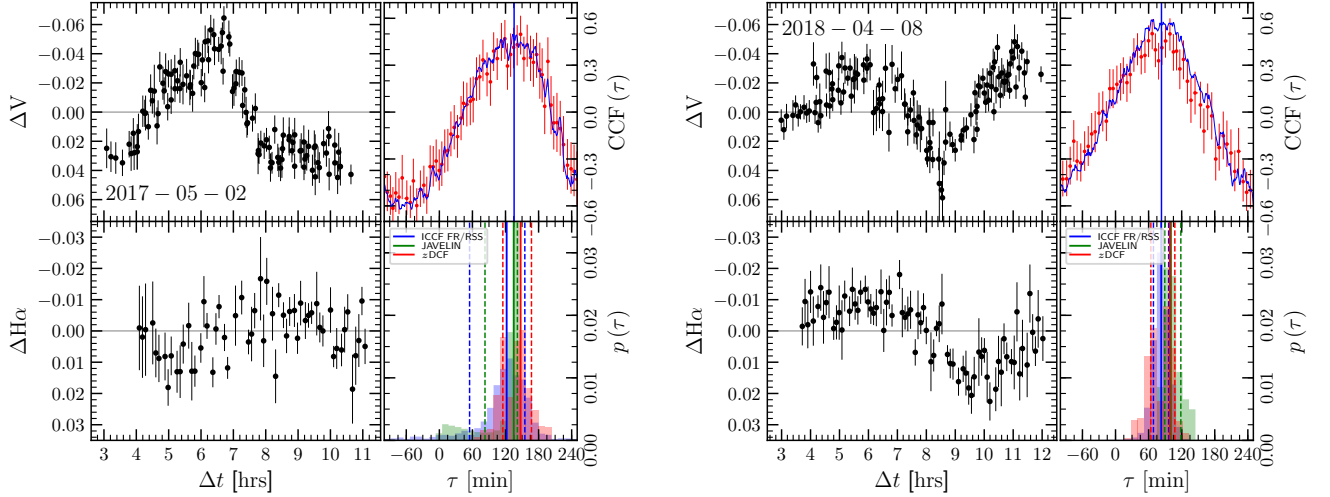


**Figure 6.** Light curves and corresponding ICCF centroid and JAVELIN results, using the data from 2017-05-02 (*left set*) and 2018-04-08 (*right set*). Each set of figures consists of 4 panels as follows; *Left*: V (*top*) and H $\alpha$  (*bottom*) light curves, where H $\alpha$  light curve is after correction for continuum contamination described in 3.3. *Top Right*: ICCF (blue) and zDCF (red) of the data, where the ICCF centroid is represented as vertical line. *Bottom Right*: Probability distributions of ICCF centroids (blue), JAVELIN models (green), and zDCF (red) for the data. Solid vertical lines mark the median (for ICCF and JAVELIN) or maximum likelihood lag (for zDCF) with dashed lines marking their central 68% intervals.

$33^{+24}_{-27}$  min. (zDCF) and  $68^{+11}_{-22}$  min. (JAVELIN) were measured for the 2018-04-08 data.

Although the quality of the light curves is much lower, we also tried to measure the time lag using the light curves from other dates, including Apr 29, Apr 30, and May 1 2017. As summarized in Table 4, the obtained time lag from these dates suffers large uncertainty due to the poor data quality and the limited time baseline, and the lack of strong variable features. Nevertheless, we find that the lag measurements are broadly consistent with that of the best light curves from 2018-04-08.

Second, we used the light curves from the best two dates, to test the effect of the continuum variability in the H $\alpha$ -band on the time lag measurement. Assuming the variability amplitude of the continuum in the H $\alpha$ -band is 25%, 50%, 75%, and 100% of that of V-band, we subtracted the continuum contribution from the total flux observed with the H $\alpha$  filter, which was on average 18.3%, but slightly varied as the V-band light curve. The continuum flux observed through the H $\alpha$  filter generally decreases the time lag between V-band continuum and H $\alpha$  line since the continuum in the V-band as well as in the H $\alpha$ -band has the same variability pattern. Thus, if we assume a smaller variability amplitude of the continuum, continuum variability signal is less subtracted from the H $\alpha$ -band light curve, weakening the variability pattern of the H $\alpha$  emission line flux. For example, we can obtain a lower limit of the lag if we do not correct for the continuum variability (i.e., assuming 0% variability amplitude) in the H $\alpha$ -band light curve.

As shown in Figure 7, the time lag increases by almost a factor of two with the maximum correction ( $K = 1$ ). While the three analysis methods, namely, ICCF, zDCF, and JAVELIN provided somewhat different lag measurements, they are mostly consistent within the uncertainties. Using the light curves from 2017-05-02, we obtained consistent results, with an increasing time lag with the higher variability amplitude. Table 4 summarizes the time lag measurements, depending on the used light curves and the analysis method.

Assuming the variability amplitude is the same between V-band and H $\alpha$ -band, we compensated for 18.3% continuum contribution in the H $\alpha$  light curve, we found the ICCF H $\alpha$  time lag to be  $\tau_{\text{ICCF}} = 122^{+33}_{-67}$  min. on 2017-05-02 and  $\tau_{\text{ICCF}} = 83 \pm 14$  min. on 2018-04-08, which are consistent within 1- $\sigma$  errors. We also conducted ICCF measurements with H $\alpha$  light curves compensating for 18.0% and 18.6% continuum, which are 1- $\sigma$  error bound for continuum fraction in narrow-band H $\alpha$  filter, but found the difference in time lag is not larger than 1 minute, thus the uncertainty arising from the error in continuum contamination measurement can be ignored.

On the other hand, we did find difference in the time lag measurement if the variability amplitude of the continuum in H $\alpha$  filter is different from that of the V-band filter, as shown in Figure 7. We also checked the consistency between ICCF and zDCF or JAVELIN time lags. We found that zDCF time lags are consistent with ICCF lags within 1- $\sigma$  interval. JAVELIN time lags seem to be

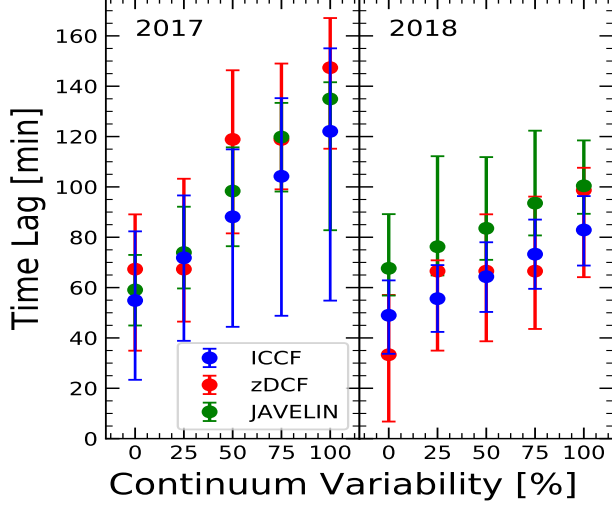


**Figure 7.** Effects of continuum variability on time lag determination. Time lags determined from ICCF (blue), zDCF (red), and JAVELIN (green) when the continuum variabilities in the  $H\alpha$  narrow-band light curves are assumed to be some fractions of that of V band for 2017(Left) and 2018(Right). Continuum fraction is assumed to be 18.3%.

systematically larger than those of ICCF and zDCF, though the difference is within  $1\text{-}\sigma$  bound.

As a consistency check for the  $H\alpha$  time lag, we also used the light curves from 3 nights, 2017-04-29, 2017-04-30, and 2017-05-01. Since these light curves showed relatively large flux uncertainties due to bad weather, we did not correct for the continuum contribution and measured the time lag of the  $H\alpha$ -band light curve with respect to the V-band light curve as shown in Figure 8. For these measurements, we only used the  $H\alpha$ -band data from the MDM 1.3m by excluding the low-quality data with large errors from the BOAO 1.8m. The measured time lags from 2017-04-29 and 2017-04-30 have large uncertainties as expected and roughly consistent with the best lag measurement from 2018-04-08 within the error. In the case of 2017-05-01, we obtained a time lag consistent with zero, presumably due to the lack of strong pattern in the light curves.

During the campaign on 2017-04-29, we obtained spectroscopic monitoring data with the Gemini GMOS for  $\sim 3.5$  hours and constructed a light curve of the  $H\alpha$  emission line. By cross-correlating with the V-band light curve, we measured the time lag as shown in Figure 9. Note that the flux calibration has large uncertainties since the sky condition was quickly changing during the campaign, which had to be ended after  $\sim 3.5$  hours. We calibrated the flux of the broad  $H\alpha$  emission line, by assuming the [SII] emission line flux is constant. Then, we converted the line flux to magnitude units for con-

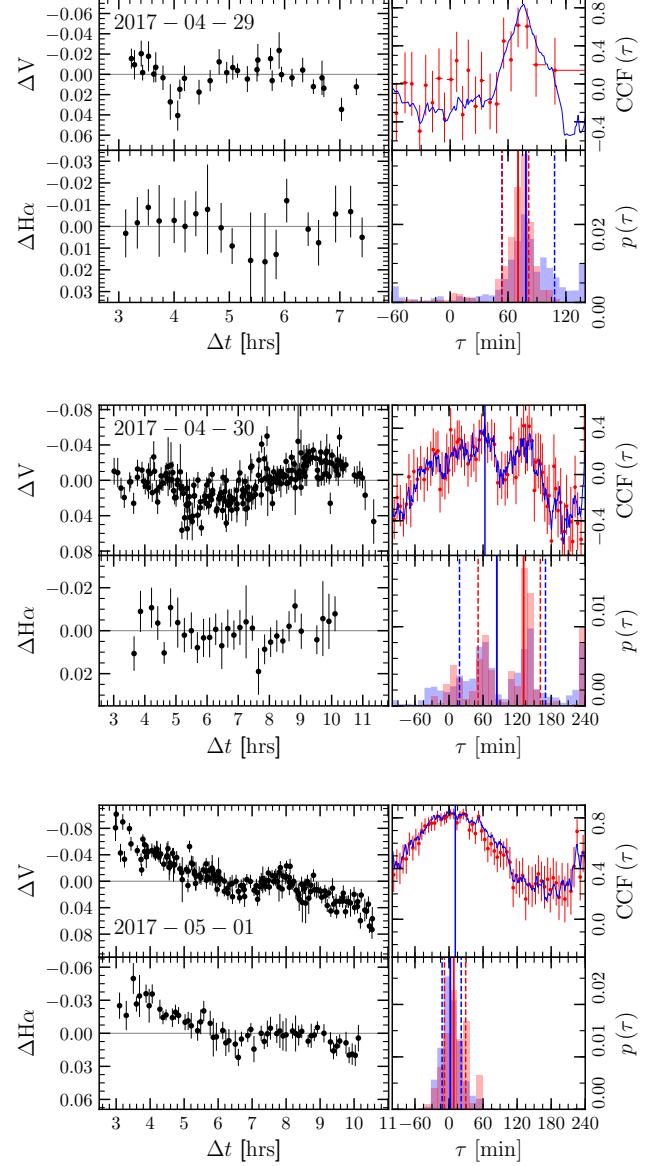


**Figure 8.** ICCF between V band and raw narrow-band  $H\alpha$  light curves. From top to bottom, each set of figures shows the ICCF analysis result for 2017-04-29, 2017-04-30, and 2017-05-01 without correcting for continuum variability in  $H\alpha$  light curves as follows; *Left*: V (top) and  $H\alpha$  (bottom) light curves, where  $H\alpha$  light curve is without correction for continuum contamination. *Top Right*: ICCF of the data, where the centroid is represented as vertical line. *Bottom Right*: Probability distributions of ICCF centroids (blue) and zDCF (red) for the data. Solid vertical lines mark the median (for ICCF) or maximum likelihood lag (for zDCF) with dashed lines marking their central 68% intervals.



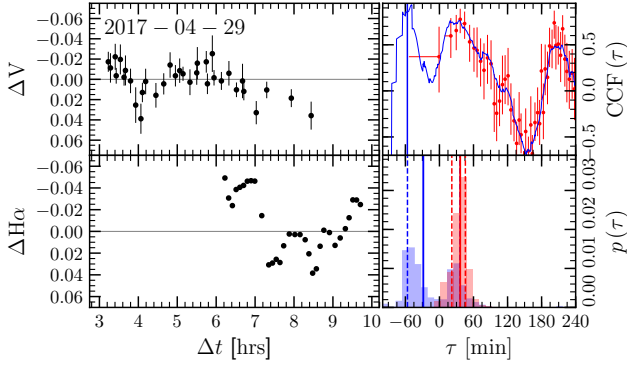


**Figure 9.** ICCF between V band and spectroscopic broad H $\alpha$  emission line flux, normalized to [SII] narrow lines. *Left:* V (top) and broad H $\alpha$  (bottom) light curves. Note that H $\alpha$  line flux is converted into relative magnitudes. *Top Right:* ICCF of the data, where the centroid is represented as vertical line. *Bottom Right:* Probability distributions of ICCF centroids (blue) and zDCF (red) for the data. Solid vertical lines mark the median (for ICCF) or maximum likelihood lag (for zDCF) with dashed lines marking their central 68% intervals. Note that this result is unreliable due to the flux uncertainties caused by bad weather and the limited time baseline (see 3.4).

sistency with the H $\alpha$ -band light curves. We could not obtain meaningful results since the overlap between the V-band and the H $\alpha$  light curves and the sampling were limited.

### 3.5. UV-to-IR Continuum Time Lag

We investigated the time lag between continuum bands using the UV, optical, and near-IR light curves. While all continuum light curves showed consistent variability patterns, we were not able to detect any reliable lag between two continuum bands as summarized in Table 5.

First, we performed a cross-correlation analysis using the UV and V-band light curves. However, these light curves have a couple of limitations. The UV light curve has gaps on the order of approximately an hour between epochs due to the invisibility of the target in each orbit of the *Swift*. Thus, a relatively short lag of an order of  $\sim 1$  hour is challenging to measure. In addition, the flux errors of the UVM2 band is relatively high as  $\Delta m \sim 0.05$ - $0.1$ , which is comparable to the fractional variability of the UVM2 light curve.

Second, we investigated the lag of near-IR continuum. Unfortunately, there was no time baseline when the optical and near-IR monitoring observations were performed simultaneously. Thus, we only compared among J, H, and K-band light curves. We obtained no meaningful time lag measurements among J, H, and K light curves

as their time baselines were relatively short, and the sampling and time resolution was limited (see Figure 3).

### 3.6. AGN Luminosity and the BLR Radius-Luminosity Relation

In this section, we investigate the size-luminosity relation by measuring the monochromatic luminosity at 5100Å. First, we calculate the mean V-band magnitude of the AGN from the light curve on 2018-04-08 and obtain  $V_{\text{AGN}} = 16.1$ . Second, we rescale the mean spectrum constructed from the 3.5-hour GMOS observations on 2017-04-29 by multiplying a scale factor of 0.507, in order to match the synthetic V-band magnitude measured from the mean spectrum with the photometry result  $V_{\text{AGN}} = 16.1$ . Here, we assume that the spectral shape changed insignificantly during 2017 and 2018. Then, we measure the monochromatic luminosity at 5100Å from the rescaled mean spectrum, and obtain  $\lambda L_{\lambda}(5100\text{Å}) = 1.02 \times 10^{40} \text{ erg s}^{-1}$ , after Galactic extinction correction, which was adopted as 0.05 magnitudes from Carson et al. (2015).

Note that the determined  $\lambda L_{\lambda}(5100\text{Å})$  is an upper limit of the AGN luminosity since there is a contribution from the host galaxy stellar component. To investigate the effect of host galaxy contribution, we model the radial surface brightness profile of the central source using two components: a point source and an exponential disk. For this analysis, we construct an average image using the high-quality V-band image data (i.e.,  $16 \times 180$  sec. exposure), which were obtained with the MDM 2.4m telescope on 2018-04-08. Note that we use the images from the same date, from which we measured the time lag of the H $\alpha$  emission line, in order to secure consistent measurements of the luminosity and the lag. Using the same aperture size used for the aperture photometry, we calculate the flux from a point-source to be 84% of the total flux in the aperture. If we remove the 16% contribution from the host galaxy disk, then AGN luminosity becomes  $\lambda L_{\lambda}(5100\text{Å}) = 8.52 \times 10^{39} \text{ erg s}^{-1}$ .

However, a more serious issue in measuring AGN monochromatic luminosity is the presence of a nuclear star cluster (NSC), which is a point-like source with an effective radius of less than  $0.3''$  (Carson et al. 2015). Since we cannot separate the NSC and the AGN in our images with a large seeing, we instead adopt the estimated luminosity of the NSC based on the modeling of the spectral energy distribution from Carson et al. (2015), which are  $-9.78^{+0.03}_{-0.04}$  mag. in F438W band and  $-10.48^{+0.06}_{-0.09}$  in F547M band after Galactic extinction correction, and determine the luminosity at 5100Å. After correcting the luminosity for the distance to NGC 4395 that we adopted in this work, we obtain

**Table 5.** Rest-frame Time Lags between Continuum Light Curves

Date (UT)	Telescopes	Light Curve 1	Light Curve 2	$\tau$ (min.)	Method
(1)	(2)	(3)	(4)	(5)	(6)
2017-04-30	UVOT, BOAO, DOAO, LOAO, MDM 1.3m, MLO, Nickel, WMO	UVM2	V	$66^{+277}_{-146}$ $-136^{+157}_{-11}$	ICCF zDCF
2017-05-01	UVOT, BOAO, DOAO, Hiroshima, LOAO, MDM 1.3m, MLO, Nickel	UVM2	V	$135^{+134}_{-126}$ $228^{+15}_{-259}$	ICCF zDCF
2017-04-26	CMO 2.5m	J	K	$0^{+95}_{-119}$ $-7^{+24}_{-7}$	ICCF zDCF
2017-04-28	CMO 2.5m	J	H	$-7^{+91}_{-92}$ $-33^{+47}_{-15}$	ICCF zDCF
2017-04-28	CMO 2.5m	J	K	$2^{+129}_{-145}$ $34^{+16}_{-13}$	ICCF zDCF
2017-04-28	CMO 2.5m	H	K	$24^{+122}_{-158}$ $47^{+177}_{-20}$	ICCF zDCF

NOTE—The time lag values are chosen from the medians of the distributions for ICCF, and from the maximum likelihood lags for zDCF. Central 68% intervals are taken as their uncertainties.

$\lambda L_{\lambda;\text{NSC}}(5100\text{\AA}) = 3.59 \times 10^{39} \text{ erg s}^{-1}$ . By subtracting the flux from the NSC, we determine the AGN luminosity to be  $\lambda L_{\lambda;\text{AGN}}(5100\text{\AA}) = 5.75 \times 10^{39} \text{ erg s}^{-1}$ .

To estimate the uncertainty of the AGN luminosity we include several sources of errors: 1) flux measurement error at 5100Å is 1.54%; 2) systematic uncertainty due to the conversion of the SDSS magnitudes of comparison star to the V band magnitudes is 0.01 magnitude (Jester et al. 2005); 3) the standard deviation of the mean magnitude from the V band light curve is 0.015 magnitudes; and 4) the flux measurement error of the NSC is 0.075 magnitude (Carson et al. 2015). Combining these errors, we determine  $\log \lambda L_{\lambda;5100\text{AGN}}(5100\text{\AA}) = 39.76 \pm 0.03$ , i.e.,  $\lambda L_{\lambda;5100\text{AGN}}(5100\text{\AA}) = (5.75 \pm 0.40) \times 10^{39} \text{ erg s}^{-1}$ .

By combining the monochromatic luminosity at 5100Å and the best measurement of the H $\alpha$  lag,  $\tau = 83 \pm 14$  min., we compare NGC 4395 with other reverberation-mapped AGNs in the size-luminosity relation (Figure 10). NGC 4395 offsets by 0.48 dex from the size-luminosity relation defined by more luminous AGNs (Bentz et al. 2013, case for *Clean+ExtCorr* in Table 14). If we consider the intrinsic scatter (i.e.,  $\lesssim 0.19$  dex) of the relation reported by Bentz et al. (2013), the offset is significant ( $\geq 2.5 \sigma$ ). On the other hand, the

systematic uncertainty of the AGN luminosity of NGC 4395 can be very large due to the difficulty of separating the AGN from the NCS. Note that recent reverberation studies showed that more luminous AGNs are scattered below the best-fit relation given by Bentz et al. (2013) (see §4.3 for more details).

## 4. DISCUSSION

### 4.1. Comparison with Previous Studies

There have been several previous studies on the emission line time lag of NGC 4395, and our time lag measurement is broadly consistent with these results. For example, Desroches et al. (2006) measured the H $\alpha$  line lag  $0.06^{+0.034}_{-0.030}$  days (or  $86^{+49}_{-43}$  min.) by integrating continuum-subtracted line spectra, which is consistent to our measurement, while Edri et al. (2012) measured the lag  $3.6 \pm 0.8$  hours (or  $216 \pm 48$  min.) based on photometric light curves with broad-band filter, i.e., SDSS  $g'$ ,  $r'$ , and  $i'$ . In the case of the broad-band photometry light curves, they measured auto-correlations for each light curve as well as cross-correlations for each combination of two light curves, then subtracted auto-correlation from cross-correlation to determine the lag between continuum and emission line. However, this

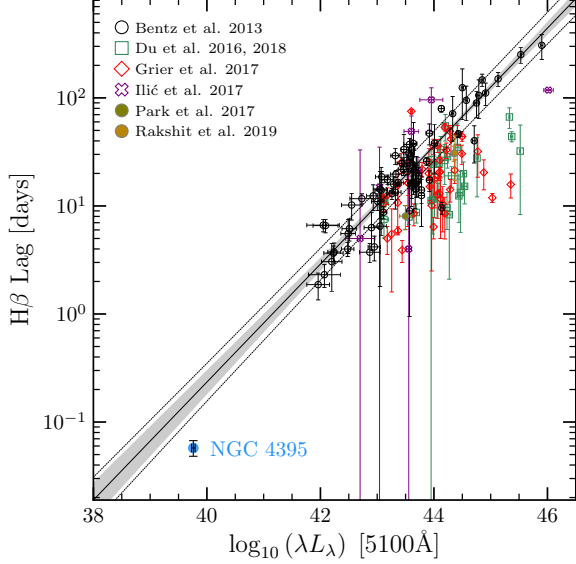


**Figure 10.** BLR radius vs. 5100Å AGN luminosity. Best fit relation by Bentz et al. (2013, *Clean+ExtCorr* in Table 14) is shown as black solid line, with shaded region indicating 1- $\sigma$  confidence interval of line fit and dotted line represent the 1- $\sigma$  prediction interval of AGNs considering intrinsic scatter. AGNs shown here are from Bentz et al. (2013), as well as Du et al. (2016, 2018), Grier et al. (2017), Ilić et al. (2017), Park et al. (2017), and Rakshit et al. (2019). NGC 4395 is shown as blue circle with black error bar.

method is less reliable since the continuum flux is dominant ( $> 75\%$ ) in the total flux measured with the broadband filters, leading to the difficulty that the flux measurement is more prone to photometric errors. Lastly, Peterson et al. (2005) reported the lag between continuum at 1350Å and the C<sub>IV</sub>λ1549 broad emission line as an order of one hour based on two different sets of light curves. The C<sub>IV</sub> lag is shorter than our H $\alpha$  lag, indicating that these measurements are consistent with the stratification of the BLR.

In the case of AGN luminosity, Filippenko & Ho (2003) reported  $L_{5100} = 6.6 \times 10^{39} \text{ erg s}^{-1}$ , which is close to our estimate. Other studies determined the bolometric luminosity of NGC 4395 by integrating the SED as  $1.2 \times 10^{41} \text{ erg s}^{-1}$  (Lira et al. 1999),  $1.9 \times 10^{40} \text{ erg s}^{-1}$  (Moran et al. 1999), and  $9.9 \times 10^{40} \text{ erg s}^{-1}$  (Brum et al. 2019). If we adopt the bolometric correction of 10 (Woo & Urry 2002) for the reported measurements,  $L_{5100}$  ranges from  $1.9 \times 10^{39} \text{ erg s}^{-1}$  to  $1.2 \times 10^{40} \text{ erg s}^{-1}$ , which are similar to our estimate.

The current investigation along with prior studies reporting estimates of the AGN luminosity are bound to various sources of systematic uncertainties. Note that the AGN PSF decomposition using high-quality imag-

ing data has been applied to many of the reverberation-mapped AGNs (Bentz et al. 2013). However, even the best spatial resolution of the HST imaging may not be enough to reliably separate the AGNs from the NSC with an effective radius of less than  $0.3''$ .

Although the luminosity of the AGN in NGC 4395 is two orders of magnitude lower than typical Seyfert 1 galaxies, the AGN seems to broadly follow the size-luminosity relation, indicating the same photoionization assumption is valid in the low luminosity end. Based on the black hole mass measurement from the H $\alpha$  reverberation mapping ( $9000 M_{\odot}$ , Woo et al. 2019), and the bolometric luminosity  $\log L_{\text{bol}} = 42.06$ , we determined the Eddington ratio as  $\sim 5\%$ . These results indicate that NGC 4395 is a scaled-down version of typical Seyfert 1 galaxy with an intermediate mass black hole and  $\sim 5\%$  of the Eddington accretion.

#### 4.2. Variability

We measured the variability of the AGN continuum in the V-band as  $F_{\text{var}} \approx 0.02$  and  $R_{\text{max}} \approx 1.1$  based on one-day baseline light curves. The amplitude of the variability slightly increases as  $F_{\text{var}} \approx 0.04 - 0.08$  and  $R_{\text{max}} \approx 1.2 - 1.7$  with a longer baseline of several days. These results are consistent with those of Desroches et al. (2006), who reported the variability in V-band photometry  $F_{\text{var}} = 0.019 - 0.042$  and  $R_{\text{max}} = 1.08 - 1.20$  based on single-night light curves. The variability of NGC 4395 is similar to those of other Seyfert 1 galaxies (e.g., Walsh et al. 2009). For example, the 15 AGNs with relatively low luminosity, which were monitored by the Lick AGN Monitoring Project 2011 over several month time scales, showed  $\sim 0.1$  mag. variability and  $F_{\text{var}}$  ranges from 0.02 to 0.13 and  $R_{\text{max}}$  ranges from 1.13 to 1.68 (Pancoast et al. 2019). These results imply that the variability characteristics of NGC 4395 are similar to those of other Seyfert 1 galaxies.

#### 4.3. The size-Luminosity relation of NGC 4395

We investigated the size-luminosity relation at the low-luminosity end by including our lag and luminosity measurements of NGC 4395. While the size-luminosity relation has been defined based on the H $\beta$  lag measurements, we only obtained H $\alpha$  lag measurement. Thus, the systematic difference between H $\beta$  and H $\alpha$  lags may introduce additional uncertainty.

It is not clear whether the H $\alpha$  time lag is longer than the more commonly used H $\beta$  lag for a given object. Kaspi et al. (2000) found no significant difference between continuum-to-H $\alpha$  and continuum-to-H $\beta$  time lag measurements in their reverberation sample. In contrast, H $\alpha$  is expected to show a longer time lag than H $\beta$

due to the optical-depth effect, which is manifested as the radial stratification within the BLR (Netzer 1975; Rees et al. 1989; Korista & Goad 2004). Bentz et al. (2010) provided a detailed discussion, reporting that  $H\alpha$  lag is a factor of 1.54 longer on average than  $H\beta$  lag based on the reverberation-mapping results of low- $z$  AGNs. If we assume that the  $H\beta$  lag is shorter than  $H\alpha$  lag, the offset of NGC 4395 from the size-luminosity relation becomes larger.

On the other hand, we need to consider the uncertainty of the measured AGN luminosity. The main systematic uncertainty comes from the correction for the flux from the NCS, which is not easily decomposed from the AGN. We adopted the luminosity of the NSC measured by Carson et al. (2015), which suffers large uncertainty due to the limited spatial resolution. Note that the AGN and the NSC have comparable effective radii, and even with the spatial resolution provided by the HST, the two sources were not clearly decomposed in the 2-D imaging analysis. Carson et al. (2015) argued that the degeneracy between the NSC and the AGN introduced a systemic uncertainty of 0.2 magnitudes for the luminosity of the NSC. We note that based on our high-quality GMOS spectrum we were not able to decompose the AGN power-law component and stellar component. Considering the degeneracy of the AGN and the NSC in the imaging and spectroscopy and the dependence of the flux ratio on the wavelength, the overall uncertainty of the AGN luminosity seems considerably large. Thus, we find no strong evidence that NGC 4395 is offset from the size-luminosity relation defined by more luminous AGNs.

Given the measured luminosity and size of the BLR, the offset of NGC 4395 from the size-luminosity relation is not significantly large when compared to more recent reverberation-mapping results. For example, AGNs from the studies by Du et al. (2016, 2018), Grier et al. (2017), Ilić et al. (2017) show a large scatter, and some of them are more offset than NGC 4395. Note that the AGNs in Du et al. (2016, 2018) have a high accretion rate (e.g., super-Eddington), which may be the reason for the offset from the relation. In contrast, NGC 4395 has a much lower Eddington ratio (i.e.,  $\sim 5\%$ ). On the other hand, the AGNs studied by Grier et al. (2017) are higher- $z$  objects with Eddington ratio larger than 0.1, and their luminosity may suffer systematic uncertainties due to the contribution from the host galaxies. To constrain the size-luminosity relation at the low luminosity end, it is necessary to obtain better measurements of the AGN luminosity of NGC 4395 and to investigate the scatter of the relation due to systematic effects and Eddington ratios.

## 5. SUMMARY AND CONCLUSIONS

We present observations of the variability of NGC 4395 along with reverberation-mapping results using the photometric data from the monitoring campaign, which was composed of optical observations during 5 nights in 2017 and 3 nights in 2018, UV observations during 4 nights in 2017 and near-IR observations during 3 nights in 2017.

In 2017, we measured the variability in the V-band as  $\sigma_{m,V} = 0.10$ ,  $R_{\max,V} = 1.70$ , and  $F_{\text{var},V} = 0.082$ , while in 2018, we measured  $\sigma_{m,V} = 0.05$ ,  $R_{\max,V} = 1.23$ , and  $F_{\text{var},V} = 0.047$ . In 2017, we measured fractional RMS variability for UVM2, J, H, and K band and observed a decreasing trend as wavelength increases, shown as  $F_{\text{var},\text{UVM2}} = 0.081$ ,  $F_{\text{var},V} = 0.082$ ,  $F_{\text{var},J} = 0.027$ ,  $F_{\text{var},H} = 0.016$ , and  $F_{\text{var},K} = 0.011$ . Based on the single-night long light curves, we measured the variability of V-band and  $H\alpha$  to be  $\sigma_{m,V} = 0.03$ ,  $R_{\max,V} = 1.11$ ,  $F_{\text{var},V} = 0.025$ ,  $\sigma_{m,H\alpha} = 0.01$ ,  $R_{\max,H\alpha} = 1.04$ , and  $F_{\text{var},H\alpha} = 0.001$  in 2017-05-02, and  $\sigma_{m,V} = 0.02$ ,  $R_{\max,V} = 1.10$ ,  $F_{\text{var},V} = 0.017$ ,  $\sigma_{m,H\alpha} = 0.01$ ,  $R_{\max,H\alpha} = 1.03$ , and  $F_{\text{var},H\alpha} = 0.006$  in 2018-04-08.

We performed the cross-correlation analysis using various pairs of light curves. For the time lag of the  $H\alpha$  emission line with respect to the V-band continuum, we demonstrated that the correction for the continuum in the narrow  $H\alpha$ -band filter significantly changed the lag since the variability of the continuum flux correlates with that of the V-band. Without a proper correction for the continuum contribution, the lag can be underestimated by a factor of  $\sim 2$ . Our best estimate for  $H\alpha$  lag measurement is  $83^{+13}_{-14}$  min. which is based on the light curves from 2018-04-08 after correcting for the continuum contribution in the narrow  $H\alpha$ -band by assuming the variability amplitude is the same as that of the V-band light curve. The  $H\alpha$  lag measurements from other light curves from various nights are consistent with the best lag measurement, although these measurements are much less reliable due to much lower quality light curves. In the case of the UV-to-V, and among near-IR bands (J, H, K), we did not find a reliable lag measurement.

We determined the monochromatic luminosity at  $5100\text{\AA}$  of the AGN in NGC 4395, by analyzing the best imaging data and the mean spectrum from the Gemini GMOS. However, the central point source also includes the flux from a nuclear star cluster. Thus, this luminosity is an upper limit. By subtracting an estimate of the luminosity of the nuclear star cluster, we obtained  $\log_{10} \lambda L_{\lambda}(5100\text{\AA})/[\text{erg s}^{-1}] = 39.76 \pm 0.03$ , which is two orders of magnitudes lower than that of any Seyfert 1 galaxy with available reverberation mapping results.



We investigated the size-luminosity relation of NGC 4395 by comparing with more luminous type 1 AGNs, finding that the relation extends to very low luminosity. This result suggests that the naive photoionization expectation is valid in this low luminosity regime. While NGC 4395 has a very low AGN luminosity, the Eddington ratio of NGC 4395 is  $\sim 0.05$ , indicating this AGN is similar to typical Seyfert 1 galaxies. Nevertheless, the offset of NGC 4395 from the best-fit size-luminosity relation of Bentz et al. (2013) is significant by 0.48 dex ( $\geq 2.5\sigma$ ), indicating that the extrapolation of the previously defined size-luminosity relation down to intermediate-mass black holes, or low-luminosity AGNs would introduce a large systematic uncertainty in black hole mass estimates. The systematic uncertainty of the size-luminosity relation has been already noted by more recent reverberation studies (e.g., Du et al. 2016, 2018; Grier et al. 2017). In order to define the low-luminosity end of the size-luminosity relation, it is necessary to perform reverberation analysis for additional targets with similar luminosities.

NGC 4395 is a unique object with an intermediate black hole mass ( $\sim 10^4 M_\odot$ ) and may have similar properties compared to typical Seyfert 1 galaxies. Further investigation on the detailed AGN properties, i.e., X-ray SED and gas outflows, will shed light on the understanding of intermediate-mass AGNs.

## ACKNOWLEDGMENTS

This work has been supported by the Basic Science Research Program through the National Research Foundation of Korean Government (2016R1A2B3011457), and by Samsung Science and Technology Foundation under Project Number SSTF -BA1501-05. The work of HC was supported by NRF Grant funded by Korean Government(NRF-2018H1A2A1061365-Global Ph.D. Fellowship Program). AMT, NISh, AEN, VLO thank the Program of Development of the Lomonosov Moscow State University. VLO thanks Prof. Ari Laor for useful discussions and interest to this project. DI, AK, LCP, OV gratefully acknowledge the support of the Ministry of Education, Science and Technological Development of the Republic of Serbia through projects 176001, 176004, 176005, and 176021.

## REFERENCES

- Alexander, T. 1997, in *Astrophysics and Space Science Library*, Vol. 218, *Astronomical Time Series*, ed. D. Maoz, A. Sternberg, & E. M. Leibowitz, 163, doi: [10.1007/978-94-015-8941-3\\_14](https://doi.org/10.1007/978-94-015-8941-3_14)
- Barai, P., & de Gouveia Dal Pino, E. M. 2019, *MNRAS*, 487, 5549, doi: [10.1093/mnras/stz1616](https://doi.org/10.1093/mnras/stz1616)
- Bentz, M. C., Walsh, J. L., Barth, A. J., et al. 2010, *ApJ*, 716, 993, doi: [10.1088/0004-637X/716/2/993](https://doi.org/10.1088/0004-637X/716/2/993)
- Bentz, M. C., Denney, K. D., Grier, C. J., et al. 2013, *ApJ*, 767, 149, doi: [10.1088/0004-637X/767/2/149](https://doi.org/10.1088/0004-637X/767/2/149)
- Blackburn, J. K., Shaw, R. A., Payne, H. E., Hayes, J. J. E., & Heasarc. 1999, *FTOOLS: A general package of software to manipulate FITS files*. <http://ascl.net/9912.002>
- Bohlin, R. C., Colina, L., & Finley, D. S. 1995, *AJ*, 110, 1316, doi: [10.1086/117606](https://doi.org/10.1086/117606)
- Bradley, L., Sipocz, B., Robitaille, T., et al. 2017, *astropy/photutils: v0.4*, doi: [10.5281/zenodo.1039309](https://doi.org/10.5281/zenodo.1039309)
- Breeveld, A. A., Landsman, W., Holland, S. T., et al. 2011, in *American Institute of Physics Conference Series*, Vol. 1358, *American Institute of Physics Conference Series*, ed. J. E. McEnery, J. L. Racusin, & N. Gehrels, 373–376, doi: [10.1063/1.3621807](https://doi.org/10.1063/1.3621807)
- Brum, C., Diniz, M. R., Riffel, R. A., et al. 2019, *MNRAS*, 486, 691, doi: [10.1093/mnras/stz893](https://doi.org/10.1093/mnras/stz893)
- Carson, D. J., Barth, A. J., Seth, A. C., et al. 2015, *AJ*, 149, 170, doi: [10.1088/0004-6256/149/5/170](https://doi.org/10.1088/0004-6256/149/5/170)
- den Brok, M., Seth, A. C., Barth, A. J., et al. 2015, *ApJ*, 809, 101, doi: [10.1088/0004-637X/809/1/101](https://doi.org/10.1088/0004-637X/809/1/101)
- Denney, K. D., Pogge, R. W., Assef, R. J., et al. 2013, *ApJ*, 775, 60, doi: [10.1088/0004-637X/775/1/60](https://doi.org/10.1088/0004-637X/775/1/60)
- Desroches, L.-B., Filippenko, A. V., Kaspi, S., et al. 2006, *ApJ*, 650, 88, doi: [10.1086/507263](https://doi.org/10.1086/507263)
- Du, P., Lu, K.-X., Zhang, Z.-X., et al. 2016, *ApJ*, 825, 126, doi: [10.3847/0004-637X/825/2/126](https://doi.org/10.3847/0004-637X/825/2/126)
- Du, P., Zhang, Z.-X., Wang, K., et al. 2018, *ApJ*, 856, 6, doi: [10.3847/1538-4357/aaae6b](https://doi.org/10.3847/1538-4357/aaae6b)
- Edri, H., Rafter, S. E., Chelouche, D., Kaspi, S., & Behar, E. 2012, *ApJ*, 756, 73, doi: [10.1088/0004-637X/756/1/73](https://doi.org/10.1088/0004-637X/756/1/73)
- Filippenko, A. V., & Ho, L. C. 2003, *ApJL*, 588, L13, doi: [10.1086/375361](https://doi.org/10.1086/375361)
- Filippenko, A. V., Ho, L. C., & Sargent, W. L. W. 1993, *ApJ*, 410, L75, doi: [10.1086/186883](https://doi.org/10.1086/186883)
- Filippenko, A. V., & Sargent, W. L. W. 1989, *ApJ*, 342, L11, doi: [10.1086/185472](https://doi.org/10.1086/185472)

- Gallo, E., & Sesana, A. 2019, *ApJL*, 883, L18, doi: [10.3847/2041-8213/ab40c6](https://doi.org/10.3847/2041-8213/ab40c6)
- Greene, J. E. 2012, *Nature Communications*, 3, 1304, doi: [10.1038/ncomms2314](https://doi.org/10.1038/ncomms2314)
- Greene, J. E., Strader, J., & Ho, L. C. 2019, arXiv e-prints, arXiv:1911.09678. <https://arxiv.org/abs/1911.09678>
- Grier, C. J., Trump, J. R., Shen, Y., et al. 2017, *ApJ*, 851, 21, doi: [10.3847/1538-4357/aa98dc](https://doi.org/10.3847/1538-4357/aa98dc)
- Ilić, D., Shapovalova, A. I., Popović, L. Č., et al. 2017, *Frontiers in Astronomy and Space Sciences*, 4, 12, doi: [10.3389/fspas.2017.00012](https://doi.org/10.3389/fspas.2017.00012)
- Jester, S., Schneider, D. P., Richards, G. T., et al. 2005, *AJ*, 130, 873, doi: [10.1086/432466](https://doi.org/10.1086/432466)
- Karachentsev, I. D., Sharina, M. E., Dolphin, A. E., et al. 2003, *A&A*, 398, 467, doi: [10.1051/0004-6361:20021598](https://doi.org/10.1051/0004-6361:20021598)
- Kaspi, S., Smith, P. S., Netzer, H., et al. 2000, *ApJ*, 533, 631, doi: [10.1086/308704](https://doi.org/10.1086/308704)
- Korista, K. T., & Goad, M. R. 2004, *ApJ*, 606, 749, doi: [10.1086/383193](https://doi.org/10.1086/383193)
- Kormendy, J., & Ho, L. C. 2013, *Annual Review of Astronomy and Astrophysics*, 51, 511, doi: [10.1146/annurev-astro-082708-101811](https://doi.org/10.1146/annurev-astro-082708-101811)
- Lira, P., Lawrence, A., O'Brien, P., et al. 1999, *MNRAS*, 305, 109, doi: [10.1046/j.1365-8711.1999.02388.x](https://doi.org/10.1046/j.1365-8711.1999.02388.x)
- Massey, P., & Gronwall, C. 1990, *ApJ*, 358, 344, doi: [10.1086/168991](https://doi.org/10.1086/168991)
- Massey, P., Strobel, K., Barnes, J. V., & Anderson, E. 1988, *ApJ*, 328, 315, doi: [10.1086/166294](https://doi.org/10.1086/166294)
- Mezcua, M., Kim, M., Ho, L. C., & Lonsdale, C. J. 2018, *MNRAS*, 480, L74, doi: [10.1093/mnrasl/sly130](https://doi.org/10.1093/mnrasl/sly130)
- Miller, B. P., Gallo, E., Greene, J. E., et al. 2015, *ApJ*, 799, 98, doi: [10.1088/0004-637X/799/1/98](https://doi.org/10.1088/0004-637X/799/1/98)
- Moran, E. C., Filippenko, A. V., Ho, L. C., et al. 1999, *PASP*, 111, 801, doi: [10.1086/316394](https://doi.org/10.1086/316394)
- Nadjip, A. E., Tatarnikov, A. M., Toomey, D. W., et al. 2017, *Astrophysical Bulletin*, 72, 349, doi: [10.1134/S1990341317030245](https://doi.org/10.1134/S1990341317030245)
- Netzer, H. 1975, *MNRAS*, 171, 395, doi: [10.1093/mnras/171.2.395](https://doi.org/10.1093/mnras/171.2.395)
- Nguyen, D. D., Seth, A. C., den Brok, M., et al. 2017, *ApJ*, 836, 237, doi: [10.3847/1538-4357/aa5cb4](https://doi.org/10.3847/1538-4357/aa5cb4)
- Nguyen, D. D., Seth, A. C., Neumayer, N., et al. 2018, *ApJ*, 858, 118, doi: [10.3847/1538-4357/aabe28](https://doi.org/10.3847/1538-4357/aabe28)
- . 2019, *ApJ*, 872, 104, doi: [10.3847/1538-4357/aafe7a](https://doi.org/10.3847/1538-4357/aafe7a)
- Pancoast, A., Skielboe, A., Pei, L., et al. 2019, *ApJ*, 871, 108, doi: [10.3847/1538-4357/aaf806](https://doi.org/10.3847/1538-4357/aaf806)
- Park, D., Woo, J.-H., Denney, K. D., & Shin, J. 2013, *ApJ*, 770, 87, doi: [10.1088/0004-637X/770/2/87](https://doi.org/10.1088/0004-637X/770/2/87)
- Park, S., Woo, J.-H., Romero-Colmenero, E., et al. 2017, *ApJ*, 847, 125, doi: [10.3847/1538-4357/aa88a3](https://doi.org/10.3847/1538-4357/aa88a3)
- Peterson, B. M., Wanders, I., Horne, K., et al. 1998, *Publications of the Astronomical Society of the Pacific*, 110, 660, doi: [10.1086/316177](https://doi.org/10.1086/316177)
- Peterson, B. M., Ferrarese, L., Gilbert, K. M., et al. 2004, *ApJ*, 613, 682, doi: [10.1086/423269](https://doi.org/10.1086/423269)
- Peterson, B. M., Bentz, M. C., Desroches, L.-B., et al. 2005, *ApJ*, 632, 799, doi: [10.1086/444494](https://doi.org/10.1086/444494)
- Rakshit, S., Woo, J.-H., Gallo, E., et al. 2019, *ApJ*, 886, 93, doi: [10.3847/1538-4357/ab49fd](https://doi.org/10.3847/1538-4357/ab49fd)
- Rees, M. J., Netzer, H., & Ferland, G. J. 1989, *ApJ*, 347, 640, doi: [10.1086/168155](https://doi.org/10.1086/168155)
- Reines, A. E., Greene, J. E., & Geha, M. 2013, *ApJ*, 775, 116, doi: [10.1088/0004-637X/775/2/116](https://doi.org/10.1088/0004-637X/775/2/116)
- Thim, F., Hoessel, J. G., Saha, A., et al. 2004, *AJ*, 127, 2322, doi: [10.1086/382244](https://doi.org/10.1086/382244)
- van Dokkum, P. G. 2001, *Publications of the Astronomical Society of the Pacific*, 113, 1420, doi: [10.1086/323894](https://doi.org/10.1086/323894)
- Vaughan, S., Edelson, R., Warwick, R. S., & Uttley, P. 2003, *MNRAS*, 345, 1271, doi: [10.1046/j.1365-2966.2003.07042.x](https://doi.org/10.1046/j.1365-2966.2003.07042.x)
- Volonteri, M., Haardt, F., & Madau, P. 2003, *ApJ*, 582, 559, doi: [10.1086/344675](https://doi.org/10.1086/344675)
- Volonteri, M., Lodato, G., & Natarajan, P. 2008, *MNRAS*, 383, 1079, doi: [10.1111/j.1365-2966.2007.12589.x](https://doi.org/10.1111/j.1365-2966.2007.12589.x)
- Walsh, J. L., Minezaki, T., Bentz, M. C., et al. 2009, *ApJS*, 185, 156, doi: [10.1088/0067-0049/185/1/156](https://doi.org/10.1088/0067-0049/185/1/156)
- White, R. J., & Peterson, B. M. 1994, *Publications of the Astronomical Society of the Pacific*, 106, 879, doi: [10.1086/133456](https://doi.org/10.1086/133456)
- Woo, J.-H., Cho, H., Gallo, E., et al. 2019, *Nature Astronomy*, 3, 755, doi: [10.1038/s41550-019-0790-3](https://doi.org/10.1038/s41550-019-0790-3)
- Woo, J.-H., & Urry, C. M. 2002, *ApJ*, 579, 530, doi: [10.1086/342878](https://doi.org/10.1086/342878)
- Yanagisawa, K., Shimizu, Y., Okita, K., et al. 2019, *PASJ*, 120, doi: [10.1093/pasj/psz117](https://doi.org/10.1093/pasj/psz117)
- Zu, Y., Kochanek, C. S., & Peterson, B. M. 2011, *ApJ*, 735, 80, doi: [10.1088/0004-637X/735/2/80](https://doi.org/10.1088/0004-637X/735/2/80)